*Pure Appl. Chem.*, Vol. 76, No. 9, pp. 1749–1768, 2004.


# Fundamental chemical features of complex manganites and cuprates for advanced functional materials engineering*

Yury D. Tretyakov and Eugene A. Goodilin‡

*Chemistry Faculty, Moscow State University, Lenin Hills, Moscow 119992, Russia*

*Abstract*: The existence of a tide relationship between fundamental chemical properties of either copper or manganese as 3d transition elements and advanced functional properties of related oxide materials is demonstrated using original experimental results. The complex role of ionic sizes, oxidation and spin states, and Jahn–Teller distortions is discussed in terms of the influence of these phenomena on the crystal structure, phase assemblage, microstructure, and physical properties of three key classes of modern copper- and manganese-containing materials (high-temperature superconductors, colossal magnetoresistive compounds, and 1d superionics), bringing up innovation technologies in electrical power engineering, microelectronics, spintronics, magnetic field sensing, electrode materials, and fuel cells.

## USE OF D-ELEMENTS FOR ENGINEERING NEW ADVANCED MATERIALS

Transition elements play a unique role in the design of functional materials. They provide the whole variety of practical properties needed for fast progress of humankind. The most fashionable example of ferrites [1] is only one, but not the only case of such a global influence of d-elements on the progress of ideas and devices (Table 1). The set of major phenomena determining these materials' functional properties (such as a relatively small ionic radii allowing the formation of compact oxygen polihedra in crystal structures, variable oxidation and spin states, Jahn-Teller distortions, and d-p electron hybridization in a metal-oxygen network) is a direct reflection of fundamental chemical properties typical of transition elements (Table 2). Two of the most perspective discoveries of new classes of oxide functional materials—high-temperature superconductors (HTSCs) and colossal magnetoresistive materials—have been made recently [2,3]; new applications are thought to be found for the family of framework manganites (Table 3).

HTSCs are oxide phases of exceptionally complex and variable composition; because of their extreme sensitivity to the conditions of synthesis, melt processing, and exploitation, they are referred to as chemical superconductors [4]. A unique feature of HTSCs are the superconducting planes $CuO_2$ with accumulated charge carriers provided by the charge reservoir blocks [5,6]. Bose-condensation into Cooper pairs below a critical temperature makes superconductivity arise [5]. $Nd_{1+x}Ba_{2-x}Cu_3O_z$ cuprates allowing the preparation of large-grained HTSCs with improved pinning parameters are of the highest interest for practice (Fig. 1) [4,7–10]. This system can be also considered as a model of how functional properties are affected by cation ordering [8,11–20]. In addition, processes associated with these materials design allow us to reveal the composition-treatment/structure–properties relationship, oxygen and cation nonstoichiometry of solid phases and structural phase transitions, thus enriching fundamental inorganic chemistry [4,8–10].

*Plenary lecture presented at the XVII Mendeleev Congress on General and Applied Chemistry, Kazan, Tatarstan, Russia, 21–26 September 2003. Other presentations are published in this issue, pp. 1605–1798.

‡Corresponding author: Fax: +7-(095)-939-09-98: E-mail: goodilin@inorg.chem.msu.ru

**Table 1** Application of some 3d-element materials [1]

| Element | Oxidation states | Function | Applications |
|---|---|---|---|
| Cu | +1, +2 (cuprates) | High-temperature superconductivity (HTSC) | Magnetic shielding and levitation, conductivity without loses (tapes and wires, coated conductors), permanent magnets, magnetic field sensing (SQUID), antennas and actuators, IR detectors, fault current limiters, current leads, transformators, motors |
| Cu | +1, +2 ($AE_{14}Cu_{24}O_{48}$) | Spin-ladders | Low-dimensional magnetic systems, potential superconductors |
| Mn | +3, +4 (manganites) | Colossal magneto-resistance (CMR) | Magnetic field sensors, high-capacity information storage devices, metal detectors, read heads, spintronics, fuel cells |
| Mn | +3, +4 (manganites) | Nanocells | Catalyzers, nuclear waste absorption, cathode materials, superionic conductors |
| Fe | +2, +3 (ferrites) | Spontaneous magnetization, magnetodielectrics | Memory cells (tapes, hard disks, nanowires in mesoporous structures), read and write heads, magnetic field leads, permanent magnets, transformators, antennas, magnetostriction filters and vibrators, magnetic fluids, thermoresistors, electrodes |
| Co | +3, +4 | Mixed oxygen and electron conductivity | Electrode materials, oxygen membranes |

The variety of advanced manganese-containing oxide materials [3] is connected with the ability of manganese to form complex framework and tunnel structures out of $MnO_6$ octahedra (Table 2) linked in a certain manner (Fig. 2). The diverse architecture of manganese-oxygen frameworks and the total charge on the framework are controlled by the concentration and type of extra-framework cations. The simultaneous presence of manganese atoms in different oxidation states and the possibility of electron exchange between $Mn^{3+}$ and $Mn^{4+}$ cations, in some cases, make spin and charge ordering feasible; a whole spectrum of physical properties interesting for applications appears as a result [3].

**Table 2** Characteristics of Cu and Mn elements.

| Configuration | $3d^9$ ($Cu^{2+}$) | $3d^4$ ($Mn^{3+}$) |
|---|---|---|
| d-element typical oxidation states in oxide materials | Cu(II), rarely Cu (I) or Cu(III) | Mn(III)-Mn(IV), rarely Mn(II) |
| Ionic radii | $Cu^{2+}$, CN = 6: 0.73A | $Mn^{3+}$, CN = 6: 0.64A |
| Jahn–Teller effects | yes | yes |
| CN and coordination shells in oxides | 2 (linear), 4 (rhombic), 5 (pyramidal), rarely 6 (distorted octahedra) | 6 (distorted octahedra), rarely 4 (square) or 5 (pyramidal) |
| "Chemical" electronegativity | Cu: 1.20 | Mn: 0.9 |

In particular, the discovery of colossal magnetoresistance (CMR) [3] and the prospects for its application (Tables 1, 3) maintain intense research on crystal and local structures, magnetic ordering, and mechanisms of CMR in different manganites. A study of $CaCu_xMn_{7-x}O_{12}$ as a new class of CMR materials [21–24] is of great interest, because the mechanism of magnetoresistance for these phases is not conventional, high magnetoresistances can be achieved in relatively low magnetic fields and the thermal stability of CMR effect is higher than that in other manganites, which, on the whole, improves the prospects for their practical appliactions. The temperature and field dependences of the MR in

$CaCu_xMn_{7-x}O_{12}$ phases suggest a large contribution of interdomain/intergrain tunneling magnetoresistance (TMR). In general, the magnitude of TMR depends on the microstructure, particularly, on the grain size, mutual particle orientation, and the area of intergrain boundaries. Optimization of all of these properties requires novel preparation techniques [23].

All three prospective compounds (Table 3) have been successfully prepared in the present work using general knowledge about inorganic chemistry of manganese and copper oxide compounds. These phases—$Nd_{1+x}Ba_{2-x}Cu_3O_z$ HTSCs, $Ca(Mn,Cu)_7O_{12}$ CMR compounds, and $Ba_6Mn_{24}O_{48}$ framework (nanocell) manganites—demonstrate in many cases quite similar features originating from the chemistry of copper and manganese as transition elements. Thus, this work is focused mostly on these exiting examples to reveal a number of important common approaches for the engineering of modern functional materials.

**Table 3** The studied compounds and their features.

| Feature | HTSC cuprates | CMR manganites | Tunnel manganites |
|---|---|---|---|
| Formulas | $REEBa_2Cu_3O_z$ | $Ca(Mn, Cu)7O_{12}$ | $(Li)_xBa_6Mn_{24}O_{48}$ |
| Properties below $T_c$ | Superconductivity | Colossal magnetoresistance | One-dimensional superionic conductor |
| Conductivity above $T_c$ | Bad metal | Semiconductor | |
| Events around $T_c$ | Bose condensation at ~95 K (Cooper pairs) | Ferrimagnetic ordering of Cu and Mn at ~150–350 K | – |
| Structure, Cu positions | Oxygen-deficient perovskite, B-type positions | Distorted perovskite, A-type positions | Hollandite-like, several types of tunnels |
| Cation disorder and defects | Substitutional, antisite, Vacancies | Substitutional, "antisite" | Composite structure: Ba disorder in tunnels |
| Consequences of Jahn–Teller distortions | Layered structure: REE-vacancy layer, $CuO_5$ pyramids, $CuO_4$ squares | Distorted octahedral $MnO_6$, 4 + 8 coordination of Mn(III)/Cu(II) | Complex edge-sharing $MnO_6$ units forming tunnels tunnels |
| Conduction | $CuO_2$ planes | Mn–O–Mn network | |
| Charge carrier doping method | Oxidation of $CuO_{1-z}$ layer to create holes and Cooper pairs in $CuO_2$ planes | Cu/Mn heterovalent substitution to change $Mn^{3+}/Mn^{4+}$ ratio in framework | $Li^+$ intercalation in tunnels |
| Magnetic subsystems | Cu antiferromagnetic ordering in $CuO_2$ planes, REE subsystem | Cu and Mn interacting subsystems | – |
| Tunneling and devices using it | Josefson effect, SQUID | TMR, spintronics, read heads | – |
| Structure-sensitive properties | Composition and defect-sensitive $T_c$, Jc(H): anisotropy, pinning centers, biaxial texturing | Composition and defect-sensitive $T_c$, R(H)/R(H0): microstructure-dependent CMR value | Anisotropic superionic conductivity |
| Materials | Bulk ceramics, coated conductors, tapes | Thin films or composites | Bulk ceramics, whiskers |
| Crystal growth | Peritectic melt solidification, modified Chokhralsky growth | Flux or TSFZ growth | Whisker crystal growth from chloride fluxes |

## IDEAL CRYSTAL STRUCTURE AND PHYSICAL PROPERTIES

Almost all HTSCs are complex layered copper-containing oxides whose structure contains oxygen-deficient perovskite blocks (Fig. 1). It is the $CuO_2$ layers that are currently considered to be responsible for superconductivity in cuprates. In these layers, the copper atoms form a square network, whereas the oxygen atoms are placed on the lines connecting copper [4,6]. The $3dx^2–y^2$ electrons of copper and $2p$

electrons of oxygen are delocalized in the layer, and such compounds possess a metallic type of conductivity. At temperatures below the critical temperature, superconductivity arises upon doping the $CuO_2$ layers with an optimum amount of charge carriers (Fig. 3). It was experimentally established that superconductivity requires that the formal oxidation state of copper in the $CuO_2$ layers be somewhat different from +2 and lie within the range of +2.05...+2.25 for hole superconductors. The Cu–O bond length in the layer is yet another important parameter determining the superconducting properties; this is limited by 0.190–0.197 nm providing the distance of 0.380–0.394 nm between nearest copper atoms. The copper atoms can also be bonded to the oxygen atoms in neighboring layers; however, these bonds should be longer and exceed 0.22 nm. In other words, the structure of superconducting cuprates contains inequivalent Cu–O bonds, viz., strong in-plane bonds and weaker perpendicular bonds. As a consequence, HTSCs have a layered structure. Electrical neutrality requires the presence of other charge-compensating layers usually consisting of readily polarizable ions (e.g., $Ba^{2+}$) which, along with the holes in the $CuO_2$ layer, help to form the Cooper pairs upon transition to the superconducting state.

Jahn–Teller effects and heavy atom ordering play an important role for HTSCs. The former leads to flat fragments or less-coordinated copper in the structure while the latter results in local structure distortions and a charge transfer between structural blocks [6–20]. The Nd123 phase (Fig. 1) consists of superconducting (SC) and dielectric blocks. In terms of a structure description as alternate layers, the SC block is adequate to a Nd-vacancy layer flanked by two $CuO_2$ superconducting planes, the latter being oxygen-stoichiometric and concentrating holes. The charge-reservoir block is adequate to a Ba–O (apical oxygen) layer positioned between one superconducting plane and a $CuO_{1-z}$ oxygen-deficient layer. Its saturation by oxygen generates alternate oxygen chains and vacancies in the $CuO_{1-z}$ plane, results in a rhombic configuration around copper and gives rise a structure orthorhombicity, changes the copper oxidation number, and causes a charge transfer to the SC planes.

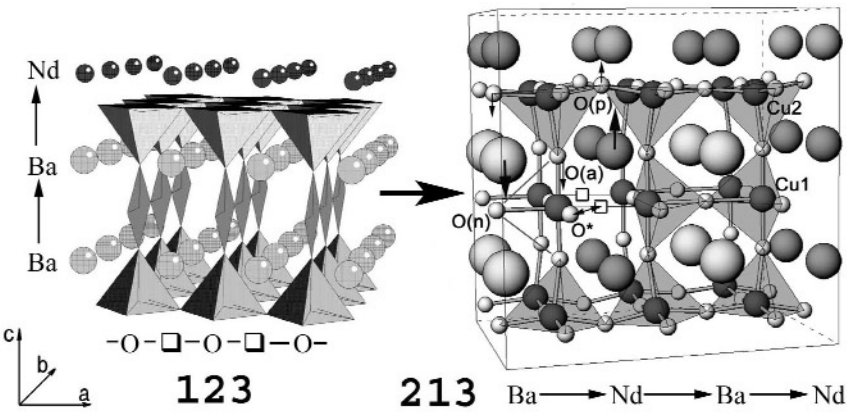


**Fig. 1** Structure of the $Nd_{1+x}Ba_{2-x}Cu_3O_z$ solid solution with various types of cation and anion ordering. "123" stands for a solid solution ($x = 0$ and $z = 7$) with an ideal crystal structure and a high critical superconducting transition temperature $T_c$ (a layer structure with ordered chains of oxygen atoms "O" and vacancies "□", left panel); "213" is a dielectric solid solution with $x = 1$, $z = 7$; O* is a position with a varied oxygen occupancy.

In the structure of $Nd_{1+x}Ba_{2-x}Cu_3O_z$ neodymium substitutes for a part of barium in barium positions. Intermediate solid solution ($0.3 < x < 0.6$, "336") is a tetragonal phase with disordered cation and anion sublattices [6]. The solid solution of the 213 type (Fig. 1) is orthorhombic over its entire range of existence, including high temperatures [7,8,11–13,17,25], because of barium and neodymium ion ordering in barium positions [12,13]. A superstructure is formed, and the primitive cell of 123 type is doubled along the c axis and in the normal direction giving a face-centered (B2*m*m) supercell. The ap-

pearance of alternate chains of barium and neodymium ions dictates oxygen ion reordering. In the high-temperature orthorhombic polymorph of the "213" phase, one of the oxygen positions along the shortest axis b is occupied only partially. In the most oxidized, ideal structure, ordered rows of $CuO_5$ pyramids could have been formed in the former [BaO] block.

$CaCu_xMn_{7-x}O_{12}$ adopts a perovskite-like structure (Fig. 2) that can be described as a framework built of tilted $MnO_6$ octahedra sharing corners [21,22]. The ordering of $Ca^{2+}$ and Jahn–Teller $Mn^{3+}/Cu^{2+}$ cations at the perovskite A-sites results in a superstructure with doubling of the perovskite lattice parameter. The Mn oxidation state on the B-site is controlled by the variation of $Cu^{2+}/Mn^{3+}$ ratio ($x$) in the solid solution. $Ca^{2+}$ ions are surrounded by 12 equidistant oxygens while $Mn^{3+}$ and $Cu^{2+}$ represent a characteristic 4 + 4 + 4 coordination due to the Jahn–Teller effect. The octahedral positions are statistically occupied by $Mn^{3+}$ and $Mn^{4+}$ ions with an average Mn–O distance of 1.945 Å.

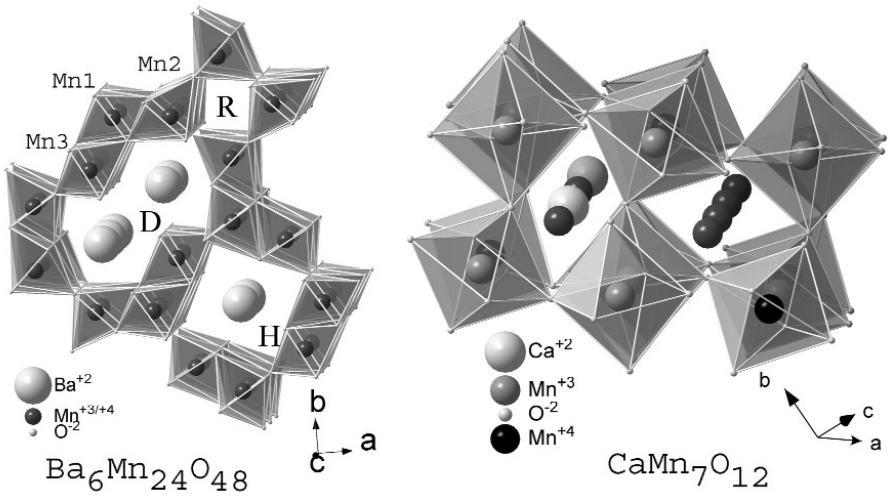


**Fig. 2** Fragments of the $Ba_6Mn_{24}O_{48}$ and $CaMn_7O_{12}$ crystal structures. The $CaMn_7O_{12}$ framework contains $Ca^{2+}$ and $Mn^{3+}$ extra-framework cations in its channels [21,22]. $Mn^{3+}$ ions also reside in distorted $MnO_6$ octahedra at the corners of the unit cell. $Mn^{4+}$ ions only occupy ideal octahedral positions. The framework of the $[Mn_{24}O_{48}]_\infty$ phase is projected on the (001) plane [26].

In the case of $Ba_6Mn_{24}O_{48}$ [26,27], the structure can be presented as a combination of two sublattices: the $[Mn_{24}O_{48}]_\infty$ framework with randomly distributed Mn(IV) and Mn(III) atoms and extra-framework $Ba^{2+}$ chains residing in channels (Fig. 2). Both sublattices have tetragonal symmetry with parameters $a \sim 18.2$ Å and $c \sim 2.8$ Å. The manganese sublattice is a combination of double columns of edge-sharing $Mn3O_6$ and $Mn1O_6$ octahedra and single columns of $Mn2O_6$ octahedra; the latter link the double columns and produce double tunnels $D$ or hollandite tunnels $H$ and also form rutile tunnels $R$. The barium sublattice is partially disordered: barium atoms in neighboring tunnels can be displaced along the $z$ axis. However, barium atom arrangement in the $D$ tunnels can have intrinsic periodicity ($c = 4.6$ Å), which is observed in domains with characteristic sizes of several nanometers. At the same time, there is no evidence of a superstructure formed by the barium atoms located in hollandite columns.

Currently, preparation of superconducting phases with a desired crystal structure and a $T_c$ above the liquid nitrogen temperature can be accomplished without any difficulty [4] as soon as optimal carrier concentration is achieved (Fig. 3). However, the attainment of high values for other important parameters (e.g., the critical current density $J_c$ and its stability in an external magnetic field) faces great difficulties for a number of reasons. The evolution from metallic to ceramic superconductors results in an increase in $T_c$ and, at the same time, in a dramatic decrease in the coherence lengths of oxide superconductors compared to those of low-temperature intermetallide superconductors (0.2 and 2 nm, re-

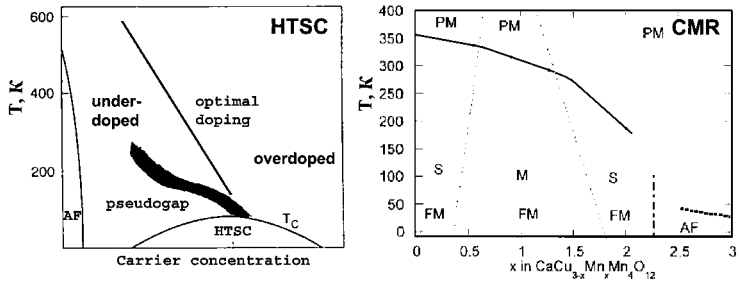


**Fig. 3** Physical phase diagrams of HTSC cuprates (left [5]) and CMR manganites (right [22]). $T_c$ – superconductivity transition temperature. AF – antiferromagnetic, PM – paramagnetic, FM – ferro- or ferrimagnetic states. M – metallic, S – semiconducting conductivity.

spectively). As a consequence, the grain boundary thickness in polycrystalline HTSC superconductors is higher than the coherence length and the superconduction current in oxide superconductors is to a great extent limited by processes occurring at grain boundaries; this is the reason why the demands imposed on the state of the intercrystallite boundary are so severe.

The situation is complicated by the fact that, because of the specific layered structure, almost all high-temperature superconducting phases possess a very high crystallographic anisotropy of physical properties, which requires texturing of polycrystalline materials. Additionally, HTSCs are type II superconductors. In an external magnetic field, they can exist in a mixed state with the magnetic flux partly penetrating the superconductor in a form of the so-called Abrikosov fluxoids. As a rule, the vortex lattice thus formed becomes more stable if extra pinning centers are generated. It is assumed that each pinning center is a distortion of the superconductor structure, the size of which is comparable with the coherence length. Generation of pinning centers is necessary since the practical use of HTSCs in the high-current devices requires not only high critical current densities ~$10^5$ Å/cm$^2$, but also enhanced current stability in external magnetic fields of 1–10 $T$ [5].

In manganites, the physical phase diagram shows strong competition between lattice, spin, charge, and orbital degrees of freedom (Fig. 3). $CaCu_3Mn_4O_{12}$ is predicted to be a small-gap magnetic semiconductor [28]. Coming from the Mn-rich end, the antiferromagnetic phase becomes a ferrimagnetic metal. In layered cuprates, shifting from an AF phase gives a metal that becomes superconducting at remarkably high temperatures 40–150 K [4]. The calculated gaps for the manganite under question are 0.50 eV for spin up (parallel to the net magnetization) and 0.18 eV for spin down. The bands at the valence-band maximum (spin down) have a strong Cu $d$ character. They are the result of antibonding interaction of $d_{xy}$ with O $p$ orbitals in the $CuO_4$ square and are the analog of $dx^2 2y^2$ states in the layered cuprates [28].

The magnetic coupling in $CaCu_3Mn_4O_{12}$ is complex due to the two types of magnetic ions of Cu and Mn aligned ferromagnetically. Both Mn and Cu ions remain magnetic but the Cu moments tend to be antiparallel to the Mn moments resulting in a ferrimagnetic spin ordering. The magnetic moment on the Cu ion is a result of the exchange splitting of the $d_{xy}$ orbital, which is the orbital with lobes pointing to the nearest-neighbor oxygens [28]. Magnetism in the Mn ion comes from the splitting of the $t_{2g}$ orbitals and filling only the spin-up states. Noncollinearity of the spins could be attributed to spin-orbital coupling. In the structure, all oxygen ions are equivalent and each one is coordinated with two Mn ions and one Cu ion. Only a single Mn–Cu coupling is important; this coupling connects a Cu spin to eight Mn neighbors and each Mn spin to six neighboring Cu spins [28].

## LOCAL STRUCTURE AND DEFECTS

Detailed studies of physical properties of all the investigated phases make us believe that there is a group of effects connected with a preparation history of the samples [8–10,14,15,17–20]. Indeed, lower synthesis temperatures of the $Nd_{1+x}Ba_{2-x}Cu_3O_y$ solid solution produce disordered solid phases whose extent of cation ordering can be controlled by varying the temperature and duration of isothermal anneal (Fig. 4). Single-phase samples showed a fairly strong dependence of $T_c$ and lattice constants on the preparation conditions. A short-term anneal in air at optimal temperatures of 980–1030 °C is sufficient to reach $T_c$ = 92–94 K. However, even 60–100 h of annealing at 900 °C finally yields $T_c$ values of at most 70 K. Clearly, plotting time-temperature-transformation (TTT) diagrams of the low-temperature region for various starting states of the solid solution (ceramics, single crystals, films) is required for the system in question. This would allow efficient control over the solid-state degradation of HTSCs, which could be employed for the targeted generation of structure microimperfections capable of acting as efficient pinning centers [7,8].

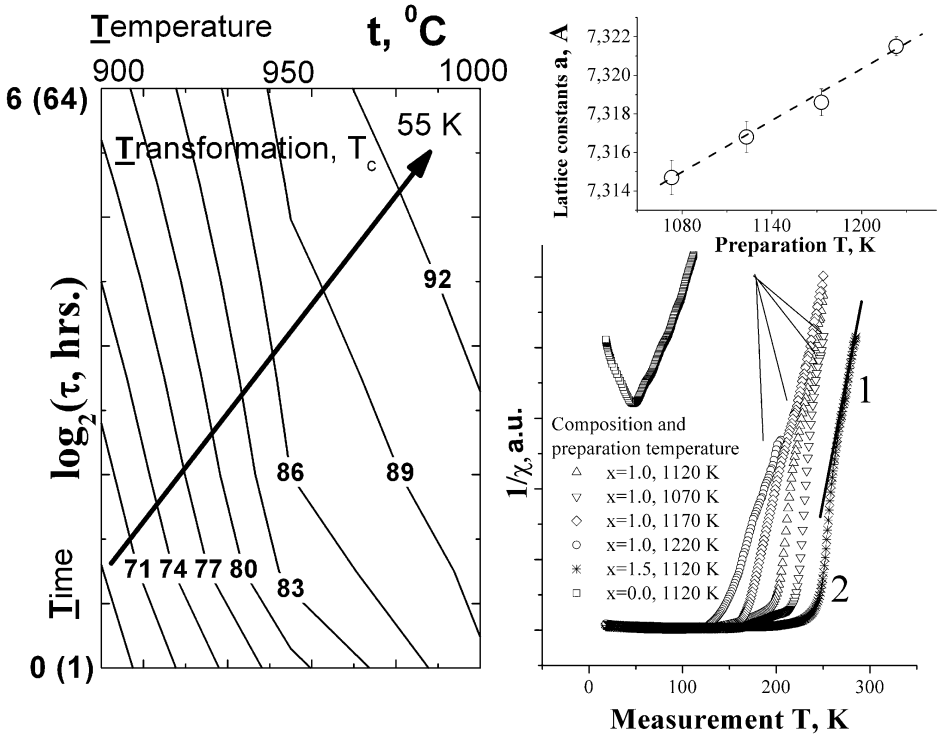


**Fig. 4** Cation disordering in solid solution-based functional materials: Time-temperature-$T_c$ diagram for the synthesis of $NdBa_2Cu_3O_z$ phase in air (left). Annealing times are given on the logarithmic scale; the final $T_c$ values after low-temperature oxidation are indicated along isolines. The 55-K arrow shows the synthesis schedule for abnormal $NdBa_2Cu_3O_z$ samples with a low $T_c$ and antisite neodymium and barium cation disordering. Inverse magnetic susceptibility as a function of temperature and lattice constants (inset) of the $CaCu_xMn_{7-x}O_{12}$ CMR phase ($0 \le x \le 1.5$) (right). "1" and "2" mark regions of the Curie–Weiss and "ferrimagnetic" behavior for the $x$ = 1 sample.

Magnetic properties of our CMR cupromanganite samples [23] are consistent with previously reported data [22]. Antiferromagnetic ordering is observed at $T_N$ = 48–49 K for $x$ = 0. The $x$ = 1 and 1.5 samples undergo magnetic ordering at $T_c$ of ~195 and 245 K, respectively (Fig. 4). The susceptibility curves of the $x$ = 1 and 1.5 samples exhibit Curie–Weiss behavior at high temperatures ("1",

Fig. 4), and show pronounced "ferrimagnetic" downward curvature in a wide temperature range ("2", Fig. 4) as extensively discussed elsewhere [22,28]. At the same time, it is easy to find (Fig. 4) that both lattice constants and critical temperatures are functions of annealing temperatures for these single-phase samples of the same composition (Fig. 4, $x = 1$, oxygen is fixed). That is an important observation since it evidences, like in the previous HTSC case and as could be expected from a general point of view, that cation ordering/disordering in a solid solution depends on preparation conditions.

It is difficult to study cation disorder by diffraction methods, in particular, by X-ray diffraction (XRD), therefore, local structure analysis methods are needed. One of them, Mössbauer spectroscopy, does not allow us to probe cation ordering directly since hyperfine parameters are dependent mostly on a first coordination sphere of iron atoms in the copper sites, i.e., surrounding oxygen. However, combinations of known types of oxygen polyhedra surrounding copper sites and their distortions are determined by the degree of Nd-for-Ba heterovalent substitution in the $Nd_{1+x}Ba_{2-x}Cu_3O_z$ solid solution. Therefore, the local structure can be assessed with a thorough comparison with known reference data. This presumably enables us to determine the type and structural consequences of cation disordering [17,18]. A number of hyperfine parameters of the solid solution correlates well with reference data grouped in several areas in Fig. 5. This grouping seems to be helpful for the spectral component identification in our experiments since the areas are separate and are predetermined by the $^{57}$Fe coordination number and the position of copper occupied by $^{57}$Fe in the structure [29].

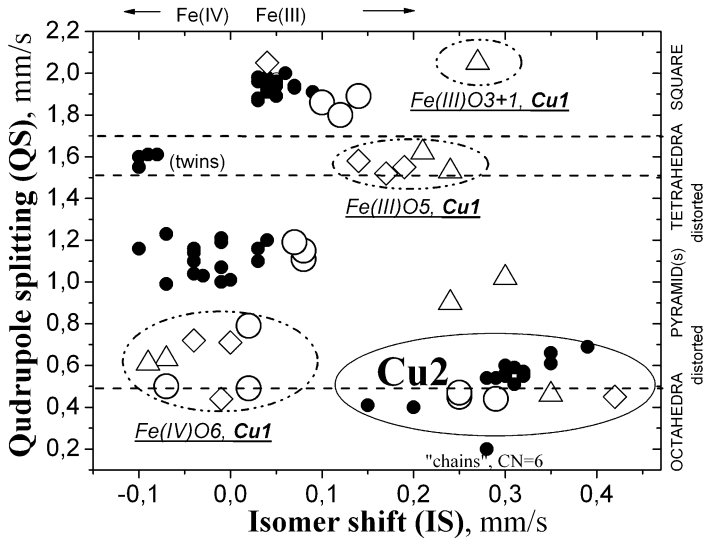


**Fig. 5** Identification of structural belongingness of iron probe atoms residing in Cu(1) chain or Cu(2) plane sites (noted with "Cu2"). Reference data on the $YBa_2Cu_3O_z$ ($z$ = 6.2–6.9) superconductor for bulk ceramics, single crystals, and thin films [29] are given as small filled circles and form several nonoverlapping areas allowing to distinguish coordination polyhedra around $^{57}$Fe. The tentative boundaries for various polyhedra corresponding some quadrupole splitting ranges are given by dashed lines. "Fe(III)" and "Fe(IV)" notations delimit isomer shift values tentatively corresponding three- and four-valent iron in the structure. Experimental data are shown as larger open symbols for $x = 0$ (circles), $x = 0.6$ (rhombs), and $x = 0.9$ (triangles).

As a consequence of Nd-for-Ba substitution, isomer shifts of spectral components become slightly larger (Fig. 5) since $Fe^{3+}$ become more stable at Cu1 sites in the solid solution because holes transfer between the charge reservoir and superconducting planes. Simultaneously, the components' quadrupole splitting increases since a displacement of apical oxygen O(3) is usually observed in the substituted solid solution. A special case of the Fe(III)O3 + 1, Cu1 component appears [17] due to a

new 3 + 1 "butterfly" oxygen configuration [2O(a) + O(n) + O*, Fig. 1] observed exclusively in the reduced Nd213:Fe solid solution with superstructural ordering of Nd and Ba [12,13].

A novel feature of both pseudocubic Nd123 and the substituted solid solution is the existence of $Fe(IV)_{Cu1}O_6$ component never observed for the reference $YBa_2Cu_3O_z$ compound. This component appears due to Nd-for-Ba substitution [18]. The $Fe(IV)_{Cu1}O_6$ octahedra are deformed as a result of asymmetry of the second coordination sphere since the second-order neighbors could be either barium atoms in their own positions or neodymium.

The increase of the iron oxidation state for this component can be explained by the formation of a $Fe(IV)_{Cu1}O_6$-$Nd_{Ba}$ defect associate (Fig. 6). In this case, the O(4) oxygen atom, supplementing the iron six-fold coordination, is stabilized by neodymium in the barium position demanding occupation of the positions in the former vacancy chains. Most likely, $Nd_{Ba}$ defects act as "anchors" for the formation of Fe(IV) octahedra in the $Cu(1)O_y$ plane. A hole in this case does not transfer into the $Cu(2)O_2$ plane or onto $Nd_{Ba}$ defects; preferably, it is caught by iron atoms in valence-saturated polyhedra forcing $^{57}Fe$ to be formally tetravalent.

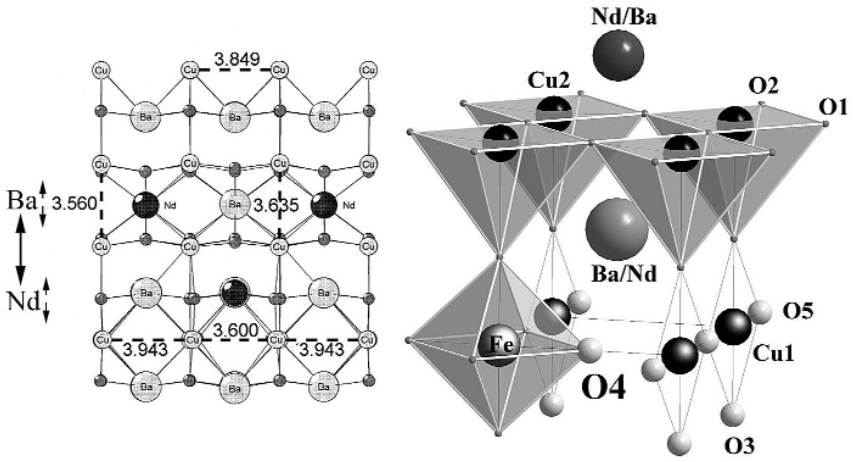


**Fig. 6** Antisite defect (left) and the $Fe(IV)_{Cu1}O_6$–$Nd^{3+}{}_{Ba2+}$ defect associate (right) models in the Nd123 phase and $Nd_{1+x}Ba_{2-x}$ $(Cu_{0.97}{}^{57}Fe_{0.03})_3O_z$ solid solution, respectively.

These results prove the possibility of a partial antisite exchange of neodymium and barium between their crystallographic positions. This is the only assumption that preserves an overall Nd:Ba:Cu = 1:2:3 phase composition, results in the reduction of c parameter of the unit cell and its orthorhombicity due to extra oxygen atoms in the former vacancy chains and local distortions of perovskite-like blocks in the structure [14,15,19,20].

The $CaMn_{6.86}Fe_{0.14}O_{12}$ spectra measured at 300 K are a superposition of two doublets with close values of chemical shifts but divergent values of quadrupole splitting [24]. As discussed, $CaMn_7O_{12}$ belongs to the $AC_3B_4O_{12}$ class of distorted perovskites. Small values of quadrupole splitting for both subspectra prove that $^{57}Fe$ cannot occupy the positions with CN = 4 + 4 + 4; therefore, all of the probe Fe(III) atoms are in the octahedral sites. Presumably, one of the components with a high quadrupole splitting is associated with those $Fe^{3+}$ cations that substitute for isovalent Jahn–Teller $Mn^{3+}$; the latter are expected to have the most distorted octahedral oxygen environment. The poorly resolved quadrupole doublet may be assigned to those $Fe^{3+}$ cations that substitute for $Mn^{4+}$ cations surrounded by almost undistorted octahedra (Fig. 2). The Mössbauer spectrum of $Ba_6Mn_{23.76}Fe_{0.24}O_{48}$ is far more complex and can be described as a superposition of four doublets (or two pairs of doublets) that have approximately equal contributions but different quadrupole splitting.

Since probe iron atoms are in the unique oxidation state of (+3), the continuum distribution of the quadrupole coupling constants can be used to describe the spectra [24]. The symmetrical and narrow character of the distribution curve of $CaMn_7O_{12}$ (Fig. 7) confirms that $Fe^{3+}$ probe cations occupy positions with similar parameters, which suggests that the nearest neighborhood is almost identical. The distortion of manganese-oxygen octahedra in the crystal structure of $Ba_6Mn_{24}O_{48}$ is evidently affected by the manner of polyhedra linkage and the degree of disorder of extra-framework barium atoms. Unlike $CaMn_7O_{12}$ with its flexible, readily deformable framework consisting of corner-sharing octahedra, the linkage of octahedra for the $Mn1O_6$–$Mn3O_6$ fragment of the $Ba_6Mn_{24}O_{48}$ phase confined to tunnels *D* and *H* (Fig. 2) is far stiffer. This imposes distortions, characteristic of the system of edge-sharing manganese-oxygen octahedra, on the probe iron atoms located in this fragment. This circumstance dictates quadrupole splitting values for probe atoms residing in the double columns. In particular, from geometrical considerations, the inhomogeneity (domainlike character) of the extra-framework barium ion distribution should cause local distortion of nearest polyhedra. The single columns, which are linked to one another only through corners and which surround vacant R tunnels, should experience the strongest deformation; the result is precisely the existence of additional spectral components. Charge redistribution in the structure caused by barium distribution inhomogeneity can only enhance similar local distortions. $Ba_6Mn_{24}O_{48}$ has a modulated structure therefore the effect of second nearest neighbors should be significant, and this would inevitably make the electric field gradient vary continuously. When the spectrum is described in a a similar manner (Fig. 7), the electric-field gradient distribution is characterized by two broadened peaks, whose position correlates with the quadrupole splitting values suggested for the probe atoms residing in double and single columns. To conclude, the parameters of Mössbauer spectral components are essential functions of the distortions of the polyhedra that exist in the intact structure and that are dictated by the linkage of framework polyhedra and the distribution of the extra-framework metal atoms in the structure.

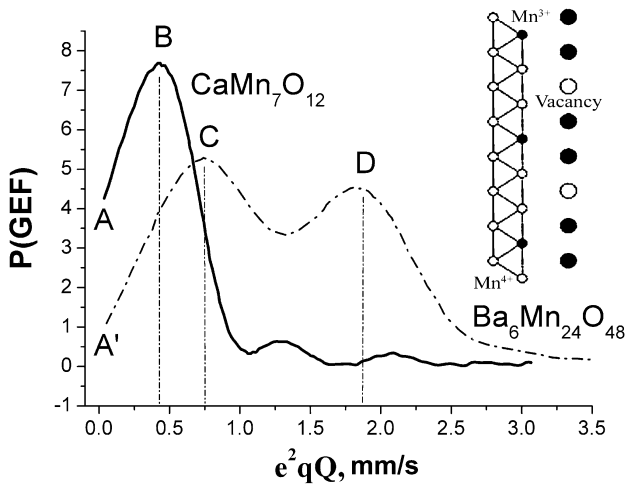


**Fig. 7** Interpretation of the Mössbauer spectra for $Ba_6Mn_{23.76}{}^{57}Fe_{0.24}O_{48}$ and $CaMn_{6.86}{}^{57}Fe_{0.14}O_{12}$ phases in terms of the model of continuum distribution (left). The composite structure of the $Ba_6Mn_{24}O_{48}$ phase (right) is reflected in the Mössbauer spectra.

## CHEMICAL PROPERTIES AND PHASE RELATIONS

The complexity of phase relations of functional materials containing transition elements can be exemplified in the family of $RBa_2Cu_3O_z$ high-temperature superconductors [7,8,13,25]. These complex cuprates are composed of such chemically different components as stoichiometric high-melting oxides

of alkaline-earth and RE elements (BaO and $R_2O_3$) and a low-melting "acidic" oxide of a transition metal (copper) in different oxidation states. As a result, the problem of oxygen nonstoichiometry arises, requiring the consideration of phase diagrams for quaternary $R_2O_3$–BaO–CuOn–$O_2$ systems with complicated "$pO_2$-temperature-composition" relations (especially in the region where the solid and liquid phases coexist). In addition, solid solutions can be formed because of rather large ionic radii of "light" RE elements (La, Pr, Nd, Sm, Eu, Gd). This complicates further the phase relations and makes optimization of the processes of preparation of HTSC materials more difficult.

Thus, the main problems are (i) the formation of nonstoichiometric (with respect to both oxygen and cations) solid solutions with a preset composition and the degree of chemical homogeneity (i.e., with a particular macroscopic and microscopic distribution of the solution components) and (ii) targeted formation of a real structure of HTSC materials, which provides the desired set of "structurally sensitive" properties. Accompanying (and sometimes no less important) problems are the investigation of the stability of this type of solid solution including the study of metastable states of high-temperature superconducting phases and their low-temperature decomposition, the prehistory effects, chemical degradation of HTSC, etc.

The $Nd_{1+x}Ba_{2-x}Cu_3O_z$ homogeneity field has a "classical" shape with two "peninsulas" at the terminal 123 and 213 solid solutions (Fig. 8). The solid solution field in the Nd–Ba–Cu–O system can be limited to $-0.1 < x < 1.0$ with the peritectic temperature peaking at $x = 0.002$–$0.1$ [8]. Likely, this is related to complex barium and neodymium ordering inside the solid solution and respective changes in the copper oxidation state (Fig. 9).

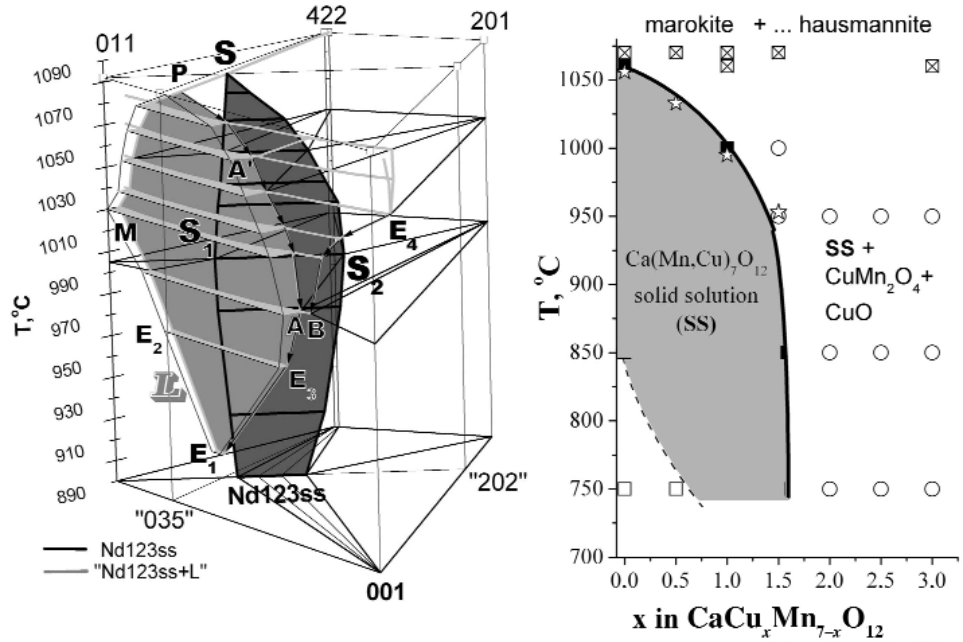


**Fig. 8** Typical phase diagrams of HTSC-cuprate and CMR-manganite solid solutions. Homogeneity region of $Nd_{1+x}Ba_{2-x}Cu_3O_z$ (Nd123ss) in air (left). $S_1SS_2$ – high-temperature boundary. L – liquid phase (light gray region $E_1E_2MPA'AE_3$ – a part of the liquid-phase loop being equilibrium with Nd123ss). 422 – $Nd_4Ba_2Cu_2O_{10}$, 201 – $Nd_2CuO_4$, 011 – $BaCuO_2$, 001 – CuO. The homogeneity field of $CaCu_xMn_{7-x}O_{12}$ solid solution at $pO_2 = 1$ bar along the $CaMn_7O_{12}$ – $CaCu_3Mn_4O_{12}$ polythermal section according to PXD, EDX, and TGA/DTA data (right). Dashed line delimits the region where $CaMn_3O_6$ and $Mn_2O_3$ are detected as impurities for $CaCu_xMn_{7-x}O_{12}$ (□).

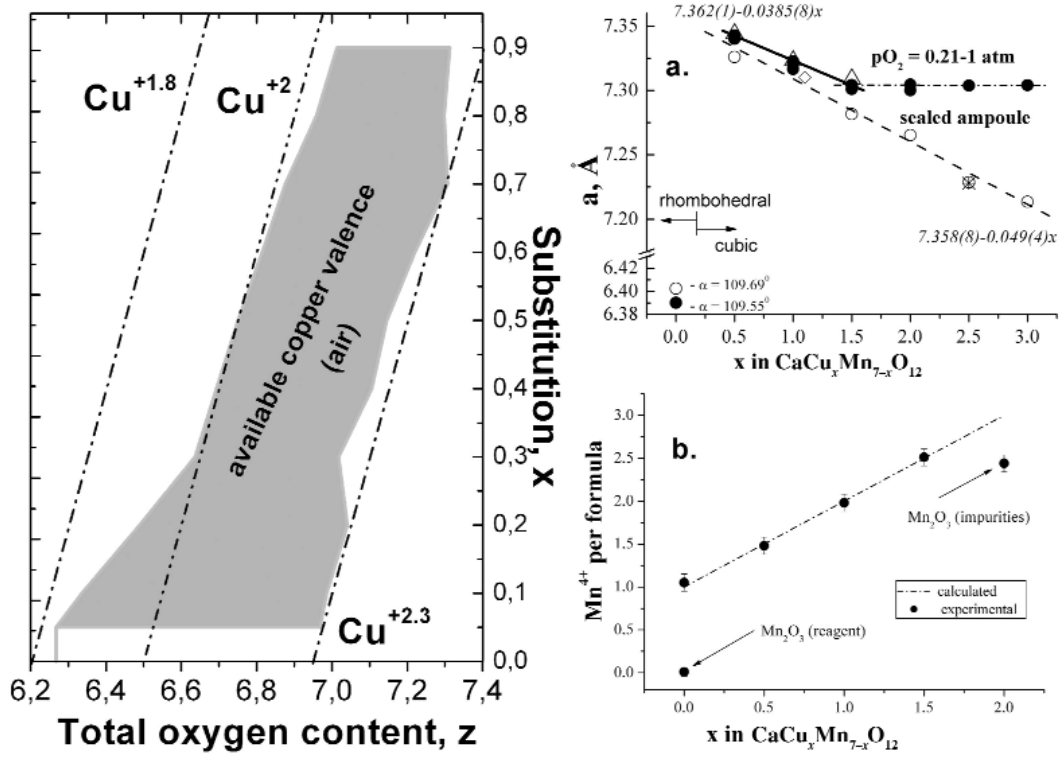


**Fig. 9** Oxidation states of copper (left) and manganese (right) in the functional materials based on $Nd_{1+x}Ba_{2-x}Cu_3O_7$ and $CaCu_xMn_{7-x}O_{12}$ phases, respectively. (a) Lattice parameters of the $CaCu_xMn_{7-x}O_{12}$ prepared under different conditions. (b) Evolution of $Mn^{4+}$ content as a function of $x$ in $CaCu_xMn_{7-x}O_{12}$ from iodometric titration data. The "$Mn_2O_3$ (reagent)" notation corresponds to titration of $Mn_2O_3$ powder used as a reagent, "$Mn_2O_3$ (impurities)" denotes titration of a multiphase sample (with $x$ = 2 nominal composition), containing $Mn_2O_3$.

A scheme of phase relations in the $CaMn_7O_{12}$–$CaCu_3Mn_4O_{12}$ polythermal section of the Ca–Mn–Cu–O system is given in Fig. 8 [23]. The $CaCu_xMn_{7-x}O_{12}$ solid solution (with different $0 \le x \le 1.5$ composition) forms in the 750 °C $\le T \le$ 1060 °C range. The homogeneity field has maximum compositional width ($x$ = 0–1.5) at ~850 °C, while it is possible to prepare the $CaCuMn_6O_{12}$ ($x$ = 1) phase in the broadest range of temperatures from 750 to 1000 °C. The "narrowing" of the $CaCu_xMn_{7-x}O_{12}$ homogeneity field at 750 °C is attributed to kinetic hindrances: the rate of phase formation decreases with decreasing Cu content. Finally, it was found that the parent $CaMn_7O_{12}$ compound decomposes at about 1060 °C into marokite $CaMn_2O_4$ and hausmannite $Mn_3O_4$. The terminating compositions of the copper-containing $CaCu_xMn_{7-x}O_{12}$ phase coexist at 750–1050 °C with $CuMn_2O_4$ and CuO.

With increasing $x$, the upper stability boundary falls from 1060 °C down to ~950 °C because of increasing $Mn^{4+}$ content. The samples prepared at 850 °C correspond to the maximal extension of the homogeneity field of $CaCu_xMn_{7-x}O_{12}$. They demonstrate substantial decrease of lattice constants in the stability range $0 < x \le 1.5$ of the cubic phase (Fig. 9). Cell constant data obey the Vegard's law and fall into a similar linear fit with a slope of about 0.04 Å per $x$ unit. This is consistent with the heterovalent substitution of $Cu^{2+}$ ions for $Mn^{3+}$ leading to a higher overall concentration of $Mn^{4+}$ (Fig. 9) and hence a decrease in the size and degree of distortion of $MnO_6$ framework octahedra in the lattice. Thus, oxidation states of copper or manganese play an important role in the phase stability of cuprates and manganites.

Additionally, HTSC rare-earth barium cuprates is the most famous example of materials with huge anion- and also cation-homogeneity fields (Fig. 10). The solid solution field can be divided into three ranges [4,8,11,12]. Compounds in the first range ($0 \le x \le 0.3$) are tetragonal after quenching from high temperatures or orthorhombic after oxidation; parameters $a$ and $c/3$ ($a < c/3$) decrease regularly due to the substitution of $Nd^{3+}$ ions for the larger $Ba^{2+}$ ions. Over the second range ($0.3 < x < 0.6$), the unit cell is tetragonal, regardless of the oxygen content ($a = c/3$). The compositions in the third range ($0.6 < x < 0.9$) show an orthorhombicity of the unit cell, as discussed above. A tight relation between the cation and anion ordering in the system of interest is evident from the T-$x$-$z$ diagram in Fig. 10. In the $x = 0$ phase, a tetra–ortho transition is a consequence of a change in the oxygen content of the phase and of the impossibility for oxygen to occur in a disordered state for above-critical concentrations. Above-critical neodymium concentrations induce barium ordering to yield the 213 phase [12]. Therefore, most oxygen in this phase is frozen in certain crystallographic positions (Fig. 1), and only "unidimensional" transition (along axis $b$) occurs between two orthorhombic 213 polymorphs. In an intermediate composition solid solution ("336"), no dominant crystallographic direction can be distinguished in the *ab* plane: the occurrence of alternate highly ordered –O–Cu–O– chains and ordered vacancy chains (as in the *ortho*-123 phase) becomes impossible since $Nd^{3+}$ ions are randomly accommodated in barium positions and force extra oxygen atoms to randomly occupy oxygen vacancies.

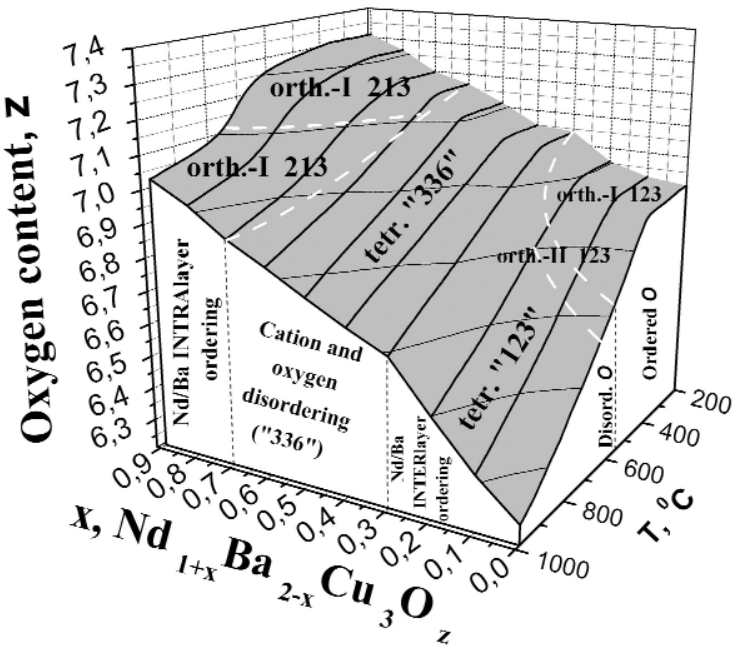


**Fig. 10** Relationship between cation and anion ordering in the $Nd_{1+x}Ba_{2-x}Cu_3O_7$ solid solution.

## PREPARATION AND MICROSTRUCTURE

The idea of designing any material is based on the concept of real structure of materials having several hierarchical levels [4]. For example, the basic crystal structure and its local distortions determine the fundamental properties (as discussed above) and are responsible for structural organization at the microscopic level. Individual crystallites, which are always imperfect and consist of smaller subcrystallites separated by extended defects (mosaic blocks, coherent scattering domains), form an intermediate mesoscopic level. Ensembles of crystallites (grains, granules) and pores form the macroscopic level (Fig. 11).

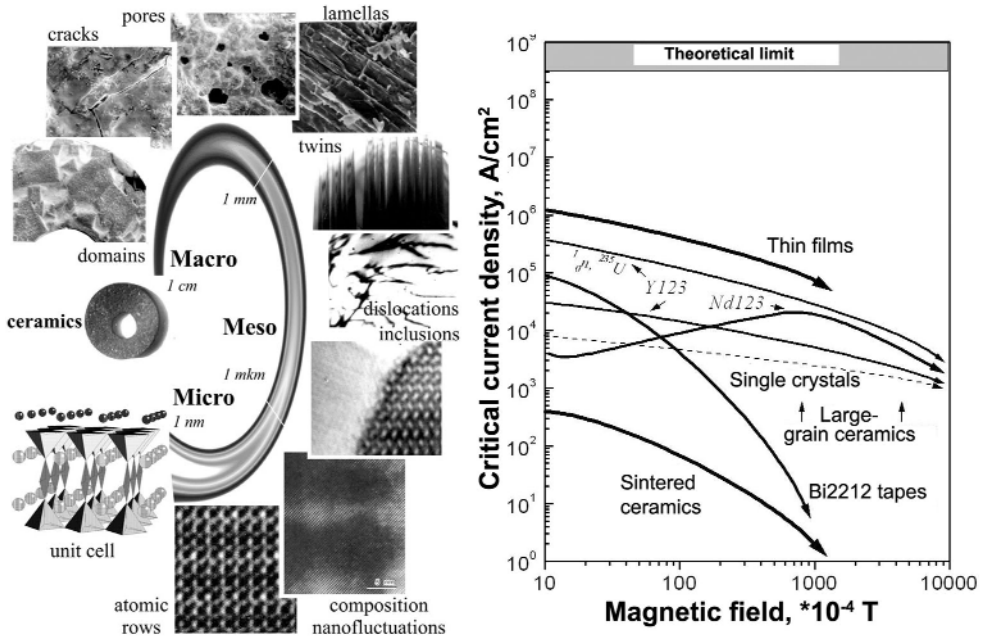


**Fig. 11** Defect hierarchy in HTSC melt-processed ceramics on macroscopic, mesoscopic and microscopic levels (left) resulting in different field dependencies of the critical current density for various superconducting materials (right).

Ensembles of large pseudo-single-crystal domains (their size reaches 0.5–5 cm depending on the precipitation conditions) separated by large-angle boundaries are the main microstructural motifs of large-grain HTSC ceramics. Each domain is a stack of thin (5–50 mm) $RBa_2Cu_3O_z$-plates or lamellae rather than a true single crystal. The lamellae are characterized by the aspect ratio of ~1000. The plates are oriented parallel to one another and are separated by low-angle boundaries, which makes them "transparent" to the critical current. The current concepts on complicated structure of melt-processed specimens of superconducting ceramics are illustrated in Fig. 11.

The real structure of melt-processed HTSCs is characterized by the presence of various extended defects such as twin boundaries, ultradisperse inclusions of nonsuperconducting phases, different types of microscopic and macroscopic cracks (which appeared due to low plasticity of the $RBa_2Cu_3O_z$ phase), and increased concentration of dislocations. The real structure of melt-processed HTSCs can be considered as a large-domain system with pronounced "collective" superconducting properties resulting in very high integral superconductivity characteristics due to the specific crystallization mechanism of the peritectic melt. "Pseudo-single-crystalline domains" are united to form macroscopic aggregates that (potentially) can carry large critical currents. Finally, a large number of defects (inclusions, dislocations, low-angle boundaries) favor the appearance of new pinning centers. In principle, all levels of structural organization of HTSC should be taken into account for enhancing its superconducting characteristics by appropriate chemical composition adjustment and carrier doping, creation of pinning centers, and achieving a microstructure with clean conducting boundaries and biaxial crystallite alignment.

Alternatively, a possibility of developing a fast (10–30 min) and low-temperature (500–600 °C) synthesis of $YBa_2Cu_3O_z$ superconductor with a $T_c$ up to 90 K appearing immediately after preparation is proposed [30]. Mechanically activated and densified two-powder precursors have reproducibly yielded 80–90 % XRD-pure $YBa_2Cu_3O_z$ phase when using internal oxygenation of dense pellets (Fig. 12) made of soft-chemistry produced $Cu_2O$ and $YBa_2O_{3.5}$ (containing $BaO_2$) treated in a planetary mill and warmly compacted at 250 °C. The advantages and unique features of this preparation

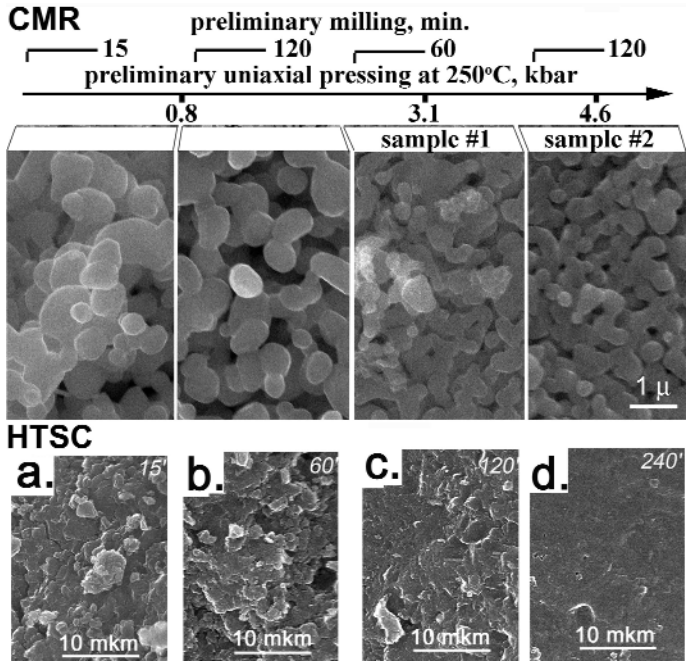


**Fig. 12** Mechanically activated and densified (MAD) preparation technique successfully applied to HTSC yttrium-barium cuprates and CMR calcium-copper manganites. An overall microstructure of raw MADTPP cuprate samples compacted at 250 °C after planetary milling is shown (left) [30]. No sintering is applied. (a) Milling for 15 min, 72 % of geometrically measured green density compared to the XRD value of Y123, (b) milling for 60 min, 75 % density, (c) milling for 120 min, 79 % density and (d) milling for 240 min, 84 % density. SEM micrographs of $CaCuMn_6O_{12}$ samples [23] prepared by MAD technique with different preprocessing conditions (milling time and pressure) as indicated in the figure, and annealed finally at 850 °C in $O_2$ for 50 h (right).

method are connected with the following: (1) the systems consist of oxides only and no gaseous products destroying local interaction contacts evolve upon the solid-state reaction of the reagents; (2) rare-earth-alkali-earth oxides concentrate cations of rare-earth elements and barium with low diffusivity, at the same time; (3) copper oxides represent the only source of copper in the system having a much better diffusion ability; and (4) different types of cations are separated in different compounds and this can provide a high gradient of chemical potentials between the reagents.

To avoid the reduction of Mn below the $Mn^{3+/4+}$ state required by stoichiometry, relatively low-temperature and/or high-oxygen partial pressure must be used for the synthesis of CMR manganites. Typically, Ca–Mn–Cu–O phases are synthesized under high-oxygen pressures (0.18–50 kbar) in evacuated silica tubes or autoclaves [21,22]. Alternatively, the mechanically activated and densified (MAD) precursor method (Fig. 12) is known to promote solid-state reactions significantly, thus allowing the preparation of these complex oxides at unusually low temperatures [2]. Moreover, mechanoactivation and densification of precursors prior to their annealing is favorable for the preparation of high-quality ceramics with enhanced transport properties [23].

It has been demonstrated above that microstructural features have a significant effect on the transport properties of HTSC ceramics. We found that a similar phenomenom takes place in the case of manganites. Although CMR is an intrinsic property of mixed-valent manganites, the grain size and intergrain boundaries can modify this response dramatically. Grain size reduction can lead to a large decrease of intrinsic CMR [31], while the increased role of grain boundaries promotes a tunneling MR originating from spin-polarized tunneling of carriers between grains [31]. The MAD technique allows

the control of the microstructure of $CaCu_xMn_{7-x}O_{12}$ samples for a given composition; this influence of microstructure on the MR properties is clearly illustrated by comparing two $CaCuMn_6O_{12}$ samples prepared under different conditions (Fig. 12). The difference in microstructures results in a 2–3 times different magnitude of MR for these samples at the same temperatures and applied magnetic fields (Fig. 13). Moreover, MR of the sample #1 is negligible above 100 K in moderate fields, while MR of ~ –5...–10 % is present at 1 *T* and 200 K for the sample #2. Since both samples were prepared from the same $CaCuMn_6O_{12}$ oxide precursor under exactly the same conditions of time, temperature, and $pO_2$ (in the same boat) and contained no impurities, the large difference in the MR magnitude is unambiguously attributed to differences in their microstructure.

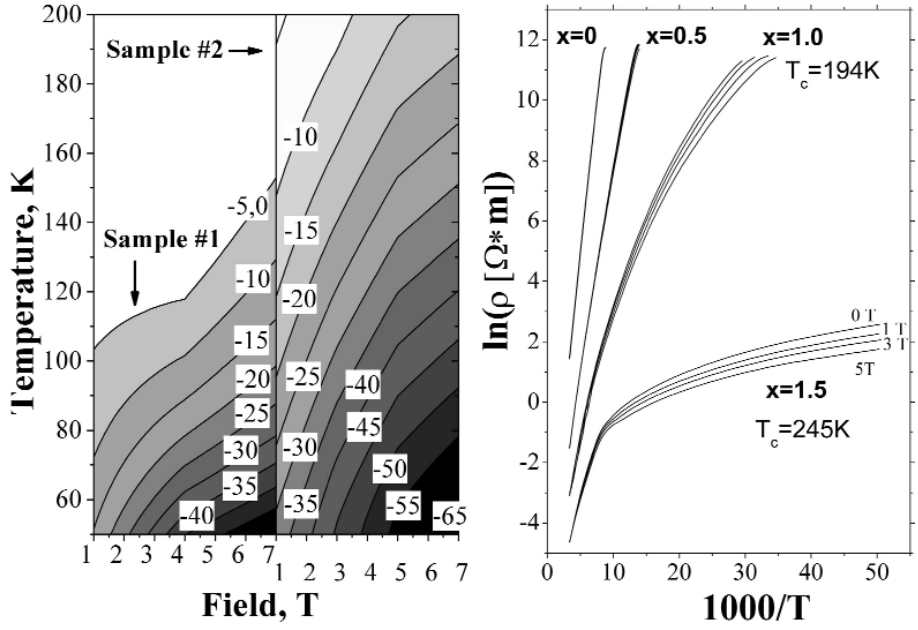


**Fig. 13** Composition and microstructure-dependent CMR properties of the MAD-processed $CaCuMn_6O_{12}$ bulk ceramics. 2D (T-H) maps of CMR response for two $CaCuMn_6O_{12}$ samples described in Fig. 12 (left). The values on isolines denote the MR magnitude in %. TMR manganites for spintronic devices. Raw Arrhenius plots of the temperature dependences of resistivity for the $CaCu_xMn_{7-x}O_{12}$ ($0 \le x \le 1.5$) samples (right). Upper curves for each series denote zero field resistance, other curves correspond to applied fields of H = 1, 3, and 5 T.

## NEW APPLICATIONS OF TEXTURED AND SINGLE-CRYSTALLINE SAMPLES

A film texture can result either from nucleation on a surface fixing both positions and orientations of the nucleii by molecular-range forces or from motion and arrangement of building blocks. Currently, the first principle is realized as vapor [4] or liquid-phase [7] heteroepitaxy on single-crystalline or biaxially textured substrates and is most commonly used in processing oriented thin films of manganite and cuprate functional materials. Although popular, it has technical limitations in terms of complicated processing, scaling for industrial production, cost effectiveness of substrates, and a detrimental limit of a small critical thickness for deposed films. The second principle of motion and arrangement of small crystals has almost no film thickness limitation as it is almost independent of the substrate nature.

To overcome a scaling problem, self-organization principles can be used for complex multicomponent systems allowing for the mutually correlated growth of all increments of such a tape. Crystals can be forced into a specific orientation if suitable geometrical constraints for their growth are imposed. For thin films, this approach is known as graphoepitaxy, which is a modification of heteroepitaxial

growth and is of great practical importance for preparation of highly oriented films of various materials on arbitrary substrates [32].

One example is the Y123 superconductor profiting from a large film thickness, e.g., in improving the engineering current and in masking the detrimental properties of underlying substrates in microwave applications. Effects of surface reliefs on texturing of its 50–100 mkm thick layers are reported recently [33–34]. $YBa_2Cu_3O_z$ crystals were biaxially aligned on untextured polycrystalline Ag–Pd substrates. Artificial surface reliefs resulted in up to 75–90 % alignment (Fig. 14). The origin of texture formation is based on various factors like topographic wall effects, crystallization pressure, surface tension, solute redistribution, and capillarity [32,33]. Possible applications of this approach for superconducting coated conductors or in the field of multiseeded substrates are highlighted [34].

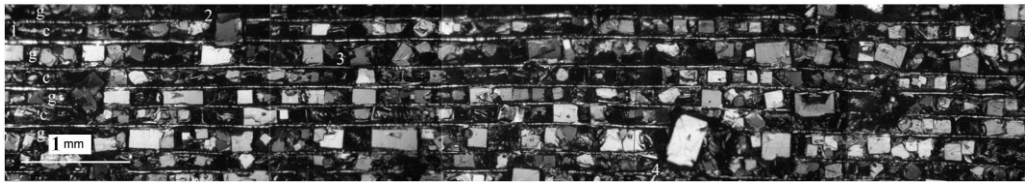


**Fig. 14** Graphotexturing of HTSC cuprate to produce long-length conducting samples. About 200 crystals are well oriented between walls along a distance of 8–9 mm (as evident from their crystal habit). White stripes are silver-alloy walls.

In order to design a new class of substrate/barrier materials, contacts, logical circuits, SQUID detectors, and other multilayer structures in HTSC microelectronics, a new generation of substrates is needed. A number of substrate materials have been used for the epitaxial deposition of HTSCs, however, no substrate material fulfills all the ideal requirements [7]. The lattice constants of Nd213 insulating crystals (Fig. 15) are very close to those of the superconducting R123 phases, and the estimated lattice mismatch is even smaller than in Pr123 and $SrTiO_3$ generally used materials [7,25,35]. The resistivity of the fully oxygenated $x = 0.85$ crystal was about 350 $k\Omega \times cm$ at 77 K, and $\varepsilon$ was found to be about 20 at 80 K (100 kHz) [35,36]. From an engineering point of view, the Nd123–Nd213 couple demonstrates two phases (a superconductor and a substrate), which can be jointly applied in the superconducting device technology. It makes Nd123ss a promising material for HTSC thin film technology [36].

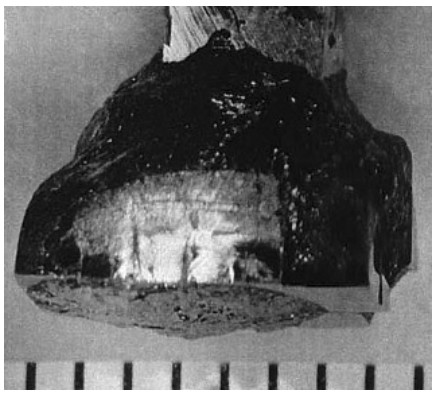

**Fig. 15** Single crystals of neodymium barium cuprate grown by the modified Chokhralsky method from peritectic melts for the production of new generations of substrate materials for superconducting thin film in modern microelectronics.

The $CaCu_xMn_{7-x}O_{12}$ phase is a possible candidate for magnetoresistive and spintronic devices [22,23]. It is evident (Fig. 13) that the conductivity of this phase varies orders of magnitude as a function of $x$. The resistivity of the $x = 0$ sample shows activated behavior with an activation energy, $E_a \sim 0.18$ eV. $E_a$ is smaller (~0.11 eV) for the $x = 0.05$ sample. The resistivities of the $x = 1$ and $x = 1.5$ (in the high-T region) samples can be fitted by Mott's law. The MR extends over a wide temperature range and increases gradually at lower temperatures and higher fields. The magnetic transitions have no pronounced signature in the resistivity data [22]. Our ceramic samples prepared by the MAD technique reproducibly demonstrate record CMR values for this system, exceeding –65 % at 35 K and 5 T [22]; this has potential technological application, e.g., as HTSC–CMR composites.

Recently, $Ba_6Mn_{24}O_{48}$ whiskers have been grown using inexpensive and nontoxic chloride fluxes (Fig. 16) [27]. As noted above, this phase has an original tunnel structure while the whisker growth direction corresponds to the direction of structural tunnels (Fig. 2). Obviously, the fibers could be a very suitable form of a raw material to compose multifilamental ceramic superionic fabrics conducting in one direction or taking part in catalytic reactions.

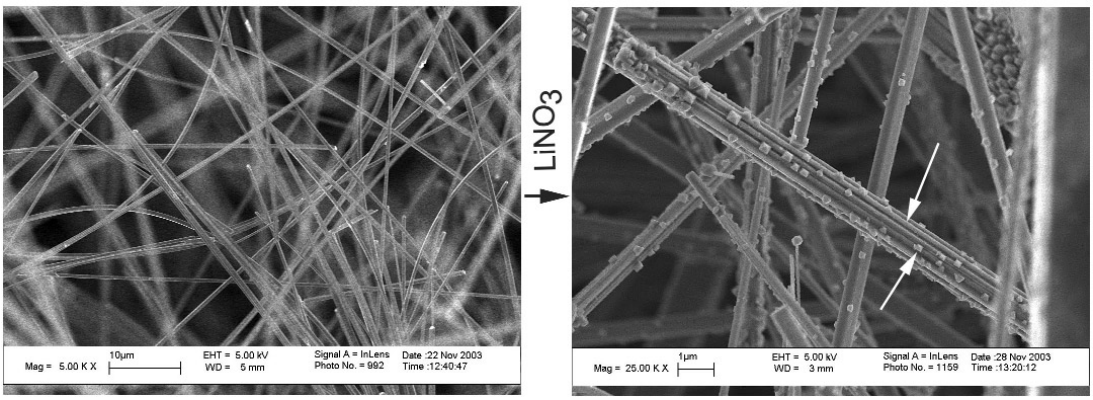


**Fig. 16** $Li_xBa_6Mn_{24}O_{48}$ one-dimensional superionic conductor (right [27]) after holding $Ba_6Mn_{24}O_{48}$ fibers grown from a chloride flux (left) in a molten $LiNO_3$ (ionic liquid). The fibers intercalate Li and partially react with the melt above 300 °C, forming oriented $Li_2Mn_2O_4$ spinel octahedra on their surface etched by the melt. The needles consist of a bunch of nanowhiskers of this framework manganite.

Thus, complicated chemistry of copper and manganese is reflected directly in fundamental physical properties of cuprate, manganite, or cupromanganite phases; this predetermines also the structural and chemical features of the phases, making it possible to predict the preparation method of the materials with desired structural and microstructural characteristics and advanced functional properties.

## ACKNOWLEDGMENTS

This work is supported by RFBR Grants 04-03-32827 and 04-03-32183, Leading Scientific School Program, Universities of Russia Fund and by the Interdisciplinary project ("New generation of magnetic materials") of Moscow State University. The authors thank G. J. Schmitz and Y. Shiohara for discussing a part of the results, D. V. Peryshkov, E. A. Pomeratseva, D. M. Itkis, I. A. Presnyakov, M. Makarova, and M. A. Novozhilov for their experimental help.

## REFERENCES


1. R. J. Cava, F. J. DiSalvo, L. E. Brus et al. *Prog. Solid State Chem.* **30**, 1–101 (2002).
2. J. G. Bednorz and K. A. Muller. *Z. Phys. B: Condens. Matter* **64**, 189 (1986).
3. C. N. R. Rao, A. K. Cheetham, R. Mahesh. *Chem. Mater*. **8**, 2421–2432 (1996).
4. Y. D. Tretyakov and E. A. Goodilin. *Russ. Chem. Rev.* **69**, 3–34 (2000).
5. B. J. Batlogg, R. Buhrman, J. R. Clem et al. *J. Supercond*. **10**, 583 (1997).
6. J. M. S. Skakle. *Mater. Sci. Eng.* **R23**, 1 (1998).
7. Y. Shiohara and E. A. Goodilin. In *Handbook on the Physics and Chemistry of Rare-Earths*, K. A. Gschneidner, Jr., L. Eyring, M. B. Maple (Eds.), pp. 67–221, Elsevier, Amsterdam (2000).
8. Yu. D. Tret'yakov and E. A. Goodilin. *Russ. J. Inorg. Chem*. **46**, S203–S234 (2001).
9. Yu. D. Tretyakov and E. A. Goodilin. *Curr. Appl. Phys*. **3**, 377–384 (2003).
10. Yu. D. Tretyakov and E. A. Goodilin. *Physica B* **321**, 249–256 (2002).
11. E. A. Goodilin, N. N. Oleynikov, G. Yu. Popov, V. A. Shpanchenko, E. V. Antipov, G. V. Balakirev, Yu. D. Tretyakov. *Physica C* **272**, 65–78 (1996).
12. E. Goodilin, M. Limonov, A. Panfilov, N. Khasanova, A. Oka, S. Tajima, Y. Shiohara. *Physica C* **300**, 250–269 (1998).
13. E. Goodilin, N. Khasanova, X. J. Wu, T. Kamiyama, F. Izumi, S. Tajima, Y. Shiohara. In *High Technology Subseries of the NATO Science Series*, Vol. 62, G. Van Tendeloo, E. V. Antipov, S. N. Putilin (Eds.), pp. 145–150, Kluwer Academic, Dordrecht (1999).
14. V. V. Petrykin, E. A. Goodilin, J. Hester, E. A. Trofimenko, N. N. Oleynikov, M. Kakihana, Yu. D. Tretyakov. *Physica C* **340**, 16–32 (2000).
15. V. V. Petrykin, E. A. Goodilin, J. Hester, E. A. Trofimenko, M. Kakihana, N. N. Oleynikov, Y. D. Tretyakov. *Physica C* **357**, 388–392 (2001).
16. M. Limonov, E. Goodilin, X. Yao, S. Tajima, Y. Shiohara, Y. Kitaev. *Phys. Rev. B* **58**, 12368–12376 (1998).
17. E. A. Gudilin, I. A. Presnyakov, M. V. Tarasov, S. N. Mudretsova, A. F. Maiorova, J. Hester, N. N. Oleinikov, Y. D. Tret'yakov. *Dokl. Chem.* **373**, 160–164 (2000).
18. K. V. Didenko, D. V. Peryshkov, E. A. Gudilin, I. A. Presnyakov, E. A. Pomerantseva, Yu. D. Tret'yakov. *Dokl. Chem*. **387**, 316–320 (2002).
19. D. V. Peryshkov, E. A. Gudilin, M. V. Makarova, E. A. Pomerantseva, S. N. Mudretsova, A. F. Maiorova, Yu. D. Tret'yakov. *Dokl. Chem*. **387**, 323–326 (2002).
20. D. V. Pyorishkov, E. A. Goodilin, M. V. Makarova, S. N. Mudretsova, A. F. Mayorova, Y. D. Tretyakov. *Dokl. Chem*. **383**, 105–109 (2002).
21. I. O. Troyanchuk, L. S. Lobanovsky, N. V. Kasper, M. Hervieu, A. Maignan, C. Michel, H. Szymczak, A. Szewczyk. *Phys. Rev. B: Condens. Matter* **58**, 14903–14907 (1998).
22. Z. Zeng, M. Greenblatt, J. E. Sunstrom, M. Croft, S. Khalid. *J. Solid State Chem*. **147**, 185–198 (1999).
23. E. A. Pomerantseva, D. M. Itkis, E. A. Gudilin, M. V. Makarova, M. B. Lobanov, N. N. Oleinikov, Yu. D. Tret'yakov. *Dokl. Chem*. **388**, 33–37 (2003).
24. E. A. Pomerantseva, D. M. Itkis, I. A. Presnyakov, E. A. Gudilin, J. Hester, N. N. Oleinikov, Yu. D. Tret'yakov. *Dokl. Chem*. **387**, 311–314 (2002).
25. E. Goodilin, A. Oka, J. G. Wen, Y. Shiohara, M. Kambara, T. Umeda. *Physica C* **299**, 279–300 (1998).
26. Ph. Boullay, M. Hervieu, B. Raveau. *J. Solid State Chem*. **132**, 239–248 (1997).
27. E. A. Gudilin, E. A. Pomerantseva, O. Y. Gorbenko, V. V. Petrykin, V. V. Poltavets, A. V. Knot'ko, A. M. Abakumov, A. V. Mironov, N. N. Oleinikov, Y. D. Tret'yakov, M. Kakihana. *Dokl. Chem*. **372**, 100–104 (2000).
28. R. Weht and W. E. Pickett. *Phys. Rev. B: Condens. Matter* **65**, 014415 (2001).

29. Z. Hommonay. "Mossbauer spectroscopy of high- Tc superconductors", in *Mössbauer Spectroscopy of Sophisticated Oxides*, A. Vertes and Z. Hommonay (Eds.), pp. 159–193, Akademiai Kiado, Budapest (1997).
30. E. A. Goodilin, D. V. Pyorishkov, A. V. Knot'ko, V. V. Lennikov, N. N. Oleynikov, Y. D. Tretyakov. *Physica C* **349**, 278–288 (2001).
31. L. E. Hueso, J. Rivas, F. Rivadulla, M. A. Lopez-Quintela. *J. Appl. Phys*. **86**, 3881–3884 (1999).
32. E. I. Givargizov. In *Handbook of Crystal Growth*, Part 3b, D. T. J. Hurle (Ed.), pp. 941–995, Elsevier, Amsterdam (1994).
33. E. A. Goodilin, E. S. Reddy, J. G. Noudem, M. Tarka, G. J. Schmitz. *J. Cryst. Growth* **241**, 512–534 (2002).
34. G. J. Schmitz, E. S. Reddy, E. A. Goodilin. *Physica C* **378–381**, 607–616 (2002).
35. E. Goodilin, F. Saba, Y. Enomoto, Y. Shiohara. *Adv. Supercond*. **X**, 717–720 (1998).
36. F. M. Saba, M. Tagami, E. A. Goodilin, Y. Shiohara, Y. Enomoto. *IEEE Trans. Appl. Supercond.* **10**, 1662–1666 (2000).